

In-flight calibration of the Swift XRT Point Spread Function

A. Moretti^a, S. Campana^a, T. Mineo^b, P. Romano^a, A.F. Abbey^c, L. Angelini^d, A. Beardmore^c, W. Burkert^g, D.N. Burrows^e, M. Capalbi^f, G. Chincarini^a, O. Citterio^a, G. Cusumano^b, M.J. Freyberg^g, P. Giommi^f, M.R. Goad^c, O. Godet^c, G.D. Hartner^g, J.E. Hill^e, J. Kennea^e, V. La Parola^b, V. Mangano^b, D. Morris^e, J.A. Nousek^e, J. Osborne^c, K. Page^c, C. Pagani^e, M. Perri^f, G. Tagliaferri^a, F. Tamburelli^f, A. Wells^c

^a INAF-Osservatorio Astronomico di Brera, Via Bianchi 46, 23807 Merate, LC, Italy

^b INAF-IASF, Via U. La Malfa 153, 90146 Palermo, Italy

^c University of Leicester, University Road, Leicester LE1 7RH, UK

^d NASA-GSFC, Greenbelt, MD 20771, USA

^e Pennsylvania State University, 525 Davey Lab, University Park, PA 16802, USA

^f ASI-ASDC, Via G. Galilei, I-00044 Frascati, Italy

^g Max-Planck-Institut für extraterrestrische Physik, Garching Germany

ABSTRACT

The *Swift* X-ray Telescope (XRT) is designed to make astrometric, spectroscopic and photometric observations of the X-ray emission from Gamma-ray bursts and their afterglows, in the energy band 0.2-10 keV. *Swift* was successfully launched on 2004 November 20. Here we report the results of the analysis of *Swift* XRT Point Spread Function (PSF) as measured in the first four months of the mission during the instrument calibration phase. The analysis includes the study of the PSF of different point-like sources both on-axis and off-axis with different spectral properties. We compare the in-flight data with the expectations from the on-ground calibration. On the basis of the calibration data we built an analytical model to reproduce the PSF as a function of the energy and the source position within the detector which can be applied in the PSF correction calculation for any extraction region geometry.

Keywords: *Swift*, XRT, PSF

1. INTRODUCTION

The *Swift* satellite¹ was successfully launched on 2004 Nov 20. The scientific payload includes one wide-field instrument, the gamma-ray Burst Alert Telescope (BAT²) and two narrow-field instruments, the X-Ray Telescope (XRT³), and the Ultraviolet/Optical Telescope (UVOT⁴). The XRT first light was on December 12th and the verification and calibration phase ended on April 5th 2005. The XRT is a sensitive, autonomous X-ray CCD imaging spectrometer designed to measure the flux, spectrum, and light curve of GRBs and their afterglows over a wide flux range covering more than seven orders of magnitude in flux in the energy band 0.2–10 keV. XRT utilizes the third flight mirror module (FM3) originally developed for the JET-X program: it consists of 12 nested, confocal and coaxial mirror shells having a Wolter I configuration. The mirror diameters range from 191 mm to 300 mm, the nominal focal length is 3500 mm, the total field of view is about 40 arcminutes (at 50% vignetting level) and the effective area at 1.5 keV is $\sim 135 \text{ cm}^2$. The XRT imaging array is a e2v technologies CCD22 consisting of 600 x 600 pixels, each $40 \mu\text{m} \times 40 \mu\text{m}$, with a nominal plate scale of 2.36 arcseconds per pixel, which makes the effective field of view of the system $\sim 24 \text{ arcmin}$.³ The whole XRT optics were also tested during the end-to-end ground calibration which was carried out at the end of 2002 at the Panter facility of the Max-Planck-Institut für Extraterrestrische Physik.⁵ Here we present the recent results of the in-flight instrument calibration phase which lasted for the first 4 months of the mission. In this period some ad-hoc observations of faint point-like sources with different spectral properties were performed in different positions of the detector in order to observe the surface brightness (SB) profile as function of the energy (E) and the

Correspondence to moretti@merate.mi.astro.it, INAF-Osservatorio Astronomico di Brera, Via Bianchi 46, 23807 Merate, LC, Italy

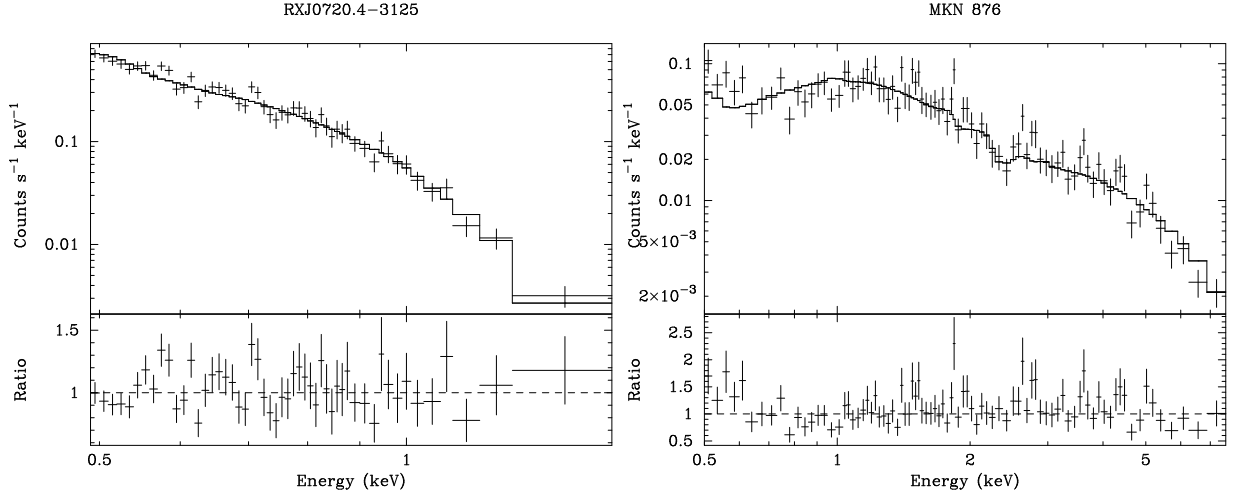


Figure 1. To study the energy dependence of the PSF we used 2 point-like sources with different spectral characteristics. The first spectrum (left panel), RXJ0720.4-3125, is well fitted by a black body model with $T_b=0.1$ keV; the second, Mkn876, is well fitted by a power law model with $\Gamma \sim 1.4$.

distance from the optical axis of the telescope, usually called off-axis angle (θ). The in-flight PSF calibration aimed to confirm that the launch and the pre-launch operations did not introduce any distortions of the optics and to measure the PSF shape with a point-like source positioned at infinite distance. The final product of this calibration is an analytical model that reproduces the SB profile of a generic point-like source and can be used for the calculation of the PSF corrections. The outline of the paper is the following. In Section 2 we describe the dataset and the data reduction procedure. In Section 3 we describe the measurements of the Half Energy Width which is a very useful parameter, commonly used to test the performance the optical systems. In Section 4 we describe the procedures we used to build and test the PSF analytical model. In the final part of this section we give an example of how the model can be used to correct an observation affected by pile-up.

2. THE DATA

Table 1. Diary of the calibration observations used in this work.

Source	Obs. ID	Off-axis angle	Exp. time(s)	Start (UT)	End (UT)
Mkn876	sw00050300004	2.0'	25676.523	2005-03-02 00:04:59	2005-03-02 23:59:40
	sw00050300005	1.7'	12730.996	2005-01-26 00:37:41	2005-01-27 21:54:41
	sw00050302001	3.2'	20760.293	2005-03-08 02:08:54	2005-03-08 23:30:40
	sw00050302002	5.0'	9438.8264	2005-03-09 00:33:52	2005-03-09 08:53:41
	sw00050303001	7.8'	6002.7062	2005-03-09 08:55:52	2005-03-09 18:47:35
	sw00050303003	6.9'	3890.0405	2005-03-12 00:50:03	2005-03-14 17:40:55
	sw00050303004	5.2'	10315.302	2005-03-24 07:07:51	2005-03-24 23:24:41
RXJ0720.4	sw00050200001	0.8'	4001.6164	2005-03-02 15:35:52	2005-03-02 23:51:42
	sw00050200003	2.6'	19782.097	2005-02-04 01:07:35	2005-02-04 23:59:41
	sw00050200005	0.1'	8509.4495	2005-05-01 01:11:30	2005-05-02 22:10:21
	sw00050202003	7.3'	15720.049	2005-03-30 02:46:47	2005-03-30 23:38:41
	sw00050203001	9.9'	18126.749	2005-02-02 00:52:58	2005-02-02 23:59:42

The XRT supports different readout modes to enable it to cover the large dynamic range and rapid variability of the GRB afterglows.⁶ The only readout mode useful for the PSF calibration purposes is the photon counting

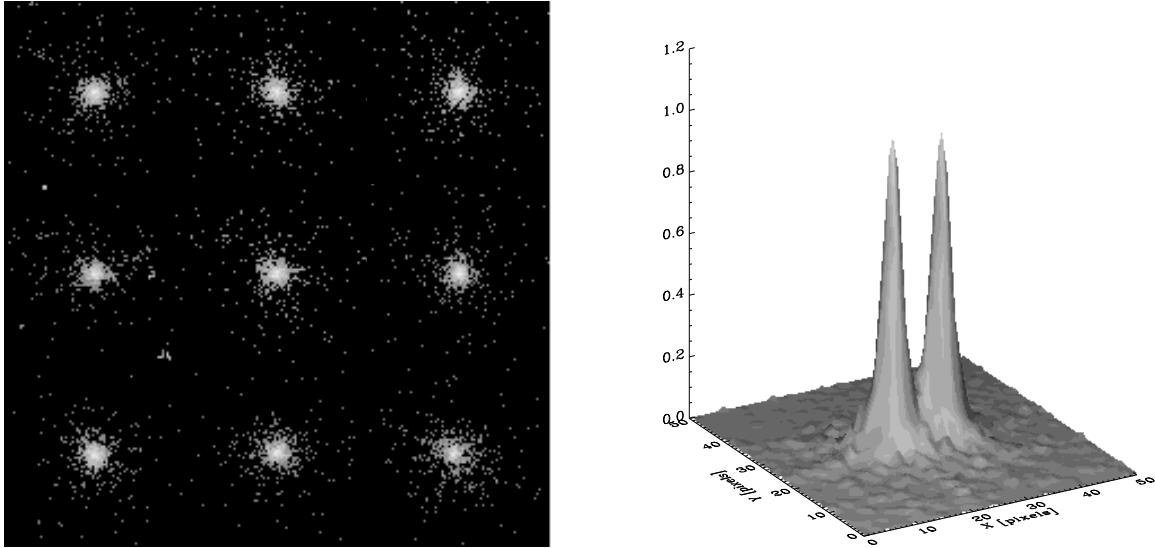


Figure 2. Some examples of the images we used in this work. Left panel. Each row corresponds to a different energy bin, 0–1(bottom), 1–2 (middle), 2–10 (top). The columns correspond to different off–axis angles in the range 1′–9′ (increasing from left to right). Right Panel. We show twice the same on–axis observation of RXJ0720.4–3125, where one image has been artificially displaced by 20″, equivalent to 8.5 pixels (1 pixel=2.36″).

(PC) mode, which allows full spectral and spatial information for source fluxes below 1 count per second. In all the paper, if not otherwise specified, we use PC data with the standard grade selection, grade 0–12. We reduced the data using the *xrtpipeline* task of the current release of the HEADAS software (version 1.4). For the PSF calibration, low count rate targets are required to completely avoid any PSF distortion due to the pile–up effect. In PC data this effect is significant for count rates > 0.7 counts per second. We used the Isolated Neutron Star RXJ0720.4–3125, which has a count rate of 0.3 counts per second in the 0.2–10 keV band, and a very soft spectrum (left panel of Fig. 1) to study the PSF at low energies (< 2 keV). In order to observe the hard energy PSF we used the observation of the active galactic nucleus Mkn 876 which has a typical count rate of 0.2 counts per seconds in the band 0.2–10keV (right panel of Fig. 1) . We have 12 useful observations (see Tab.1), 7 of Mkn876 and 5 of RXJ0720.4–3125, taken in different positions within the field of view, in the 0.1′ to 9.9′ range. To study the energy dependence of the PSF, we split the events of all the observations in 3 different energy bins, 0.2–1, 1–2, 2–10 keV (see Fig.2). This binning is a trade–off between having a good energy resolution and a significant number of photons for each bin. Note that the RXJ0720.4–3125 observations have the third energy bin completely empty (Fig.1). This resulted in a list of 31 images ($5 \times 2 + 7 \times 3$). The PSF profile analysis was performed by means of some home–made IDL routines and some DAOPHOT routines within the IDL Astronomy Library(<http://idlastro.gsfc.nasa.gov>).

3. THE HALF ENERGY WIDTH

The Half Energy Width (HEW), defined as the diameter that contains 50% of the total flux, is a very useful parameter to test the performance of our optical system and to study the dependence of the PSF on the different energies and positions in the focal plane (Tab. 2). In the left panel of Fig.3 the HEW values, measured on–axis, at the 3 different energies, are reported. In the right panel of the same figure the HEWs calculated on the 0.2–1 keV images are plotted at different off–axis angles: the HEW on–axis is a local maximum and the HEW decreases for off–axis angles up to 6′. The same feature is expected and was also observed from the ground calibration data (see the same figure). It is due to the fact that the CCD is intentionally slightly offset along the optical axis from the best on–axis focus in order to have a uniform PSF over a large fraction of the field of view. The comparison

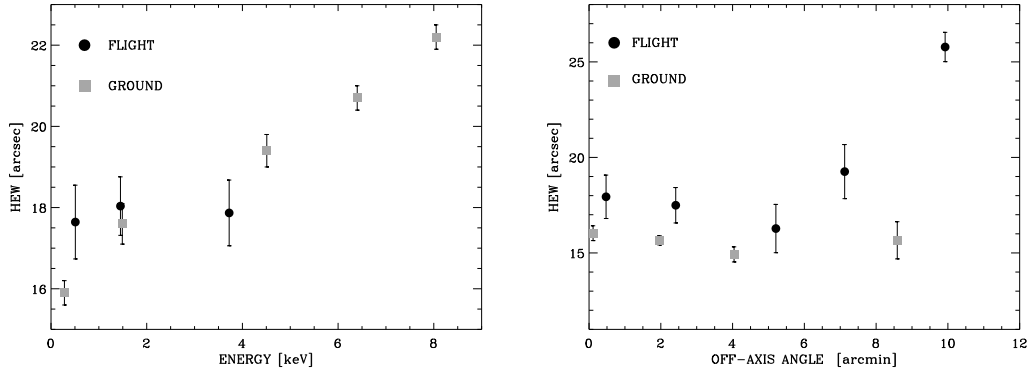


Figure 3. In the left panel the HEW on-axis measurements are plotted as a function of energy. In the right panel the HEWs measured on the low energy (0.2-1 keV) images are plotted against the distance from the optical axis of the telescope. The flight data are also compared with the on ground calibration results.

of the data with the HEWs expected from ray tracing indicated that the offset is about -2 mm.⁵ The result is that the optical response of the system is highly uniform over the central $\sim 8'$ radius region of the field of view. Because of the particular operational procedures of the satellite, many XRT observations are performed with the source not perfectly on-axis: the detector position along the optical axis represents a good trade-off between having a good spatial resolution and a larger field of view. We also note that beyond $\sim 8'$ the HEW increases considerably.

Table 2. In the table the HEW values on- and off-axis at different energies are reported. All the values are in arcseconds. We report, as a comparison, the HEW values measured from the ground calibration data.

Energy [keV]	On-axis($0'-2'$)	Off-axis($5'-7'$)	Ground on-axis	Ground off-axis($7'$)
0.5	17.6 " \pm 0.9	16.4 " \pm 1.1	15.9 " \pm 0.3	14.9 " \pm 0.4
1.5	18.0 " \pm 0.7	17.2 " \pm 0.8	17.6 " \pm 0.5	17.3 " \pm 0.7
4.0	17.8 " \pm 0.8	17.4 " \pm 0.8	19.4 " \pm 0.4	19.3 " \pm 0.2

The comparison shows that the HEWs measured in-flight are consistent with the on-ground measurements at higher energies. At the lowest energy the HEW measured in-flight, instead, is larger than the one measured on ground. In this comparison we have to take into account two important effects that can explain the differences with the in-flight PSF at very low energies. First, the HEWs reported from ground calibrations were measured from imaging mode data, for which no event reconstruction is performed. In that case the PSF directly mapped the charge distribution while there is a clear evidence that the event reconstruction slightly affects the PSF shape especially at very low energies. The imaging mode, on the other hand, does not have any spectral resolution, and since in-flight we do not have any really monochromatic source available (like on ground) we were forced to use PC mode data to study the energy dependence of the PSF. Moreover, the final aim of this study is to calculate the PSF correction for PC and Windowed Timing (WT) mode. Second, the observation performed in-flight are the sum of many different pointings. Typically there are 15 different pointings for a 20ks observation (one single pointing cannot collect enough photons to perform a statistically significant study) and the spacecraft attitude reconstruction accuracy is 3 arcseconds.

4. THE PSF ANALYTICAL MODEL

The crucial point in our PSF analysis is the construction of an analytical model which describes the PSF as function of (E, θ) . The main goal of building this model is the calculation of the PSF correction, which gives for

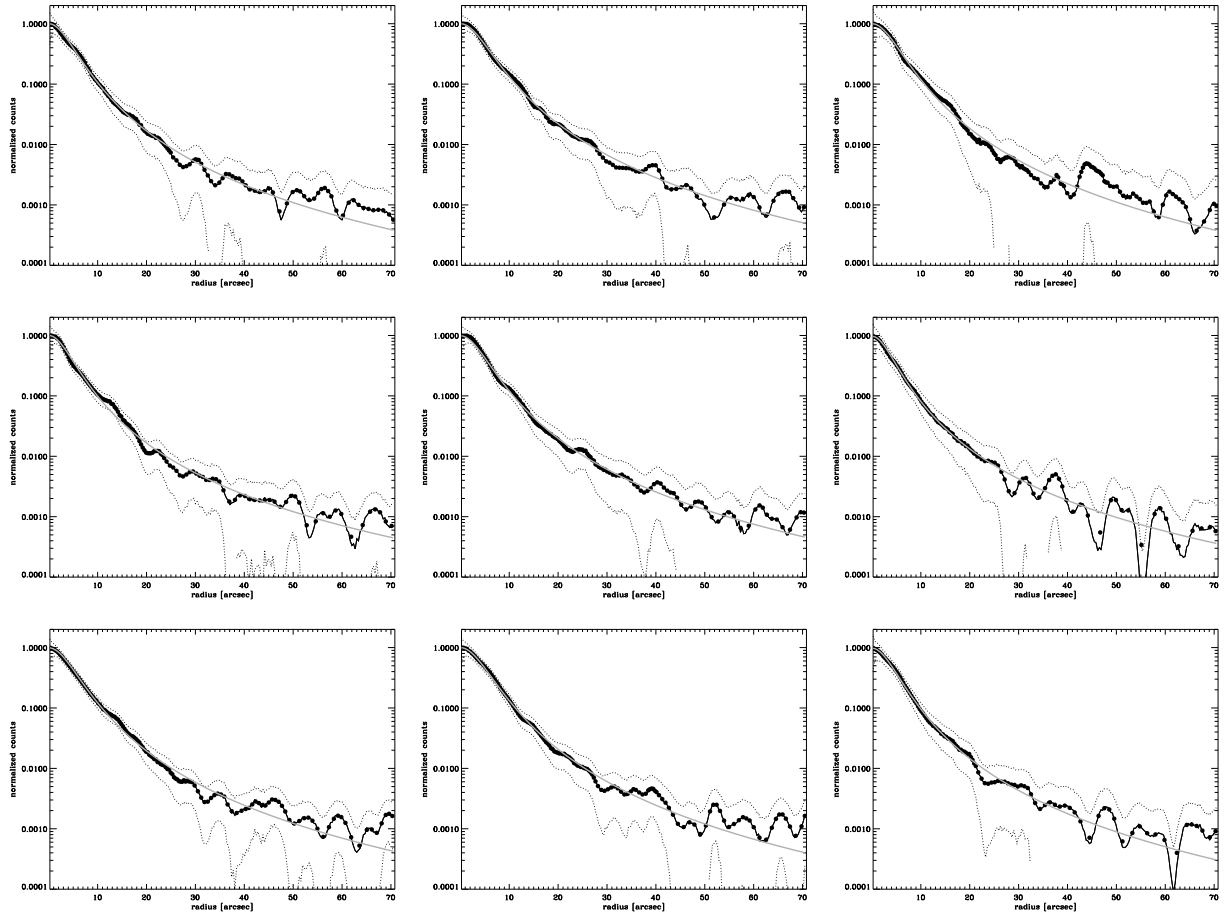


Figure 4. Mean radial profiles (black dots) in lin-log scale of the same sources shown in the left panel of Fig.2, together with their best fit by means of a King function (grey lines). The dotted lines are the error at 90% confidence.

a generic observed source the fraction of the flux contained in the extraction region with a generic shape (square, circle or annulus for example). This is a fundamental ingredient in the photometric measurements and also in the construction of the Ancillary Response File (ARF⁷) necessary for spectroscopic analysis.

4.1. Building the model

The analysis of the XRT PSF has been performed assuming a radial dependence of the PSF. In the inner PSF regions, close to the centroid, where the slope of the profile is very steep, we sampled the PSF with annuli of 1/5 pixel width. In the external part of the PSF, where the number of counts is low, we sampled the profile on scales of 5 pixels. We selected all the observations of the 2 calibration sources up to 9' of off-axis angle and for each observation we split the events in three energy bins (0.2-1,1-2,2-10 keV). As shown in Fig. 4 for each choice of energy bin and off-axis position, the PSF profile can be well fitted by a King function:

$$PSF(r) = (1 + (\frac{r}{r_c})^2)^{-\beta}. \quad (1)$$

One of the main advantages of this function is that it is analytically integrable in rdr and therefore the integral profile (or Encircled Energy Fraction, EEf) and correspondingly the total flux of a source are also analytically characterized.

$$EEF(r) \equiv \int_0^r PSF(r') 2\pi r' dr' = \frac{\pi r_c^2 (1 - W)}{1 - \beta} ((1 + (\frac{r}{r_c})^2)^{1-\beta} - 1) \quad (2)$$

$$EEF(\infty) = \pi r_c^2 / (\beta - 1) \quad (3)$$

In Fig.4, following the same scheme of Fig.2, we show 9 different SB radial profiles for different choices of spectral properties and off-axis angle with their best fit.

The model has 2 free parameters (plus the normalization), the core radius (r_c) and the slope (β) which are functions of the energy E and position, $r_c = r_c(E, \theta)$, $\beta = \beta(E, \theta)$. To make the model useful for our purposes, i.e. the PSF correction for a generic source, we need to make it predictive and we used the following procedure. For each of the different sampling points in the energy-position (E, θ) plane, we fitted the best fit PSF parameter

Table 3. The typical values of the parameter of the King function.

Energy [keV]	θ [arcmin]	r_c (")	β	XMM r_c (")	XMM β
0.5	0	5.6	1.5	4.1	1.4
0.5	7	5.0	1.4		
4.0	0	6.1	1.6	5.1	1.5
4.0	7	5.0	1.3		

values $r_c(E, \theta)$ and $\beta(E, \theta)$ with a plane function:

$$r_c(E, \theta) = a_1 + b_1 \times \theta + c_1 \times E + d_1 \times E \times \theta$$

$$\beta(E, \theta) = a_2 + b_2 \times \theta + c_2 \times E + d_2 \times E \times \theta$$

The values of the plane function coefficients are stored in the PSF file within the *Swift* XRT CALDB distribution (<http://swift.gsfc.nasa.gov/docs/swift/analysis>). In this way, given the position within the field of view and the energy for an hypothetical monochromatic source we can calculate the corresponding values of r_c and β and reproduce the PSF by means of this parametrization. To give an accurate description of the PSF profile of a source with a generic spectrum we have to sum the single monochromatic contributions. We note that the on-ground model was slightly different, since it also included a Gaussian function to take into account the very central part of the PSF (while the King function accounted for the external wings). Fitting the in-flight data with the King function only we obtained the same χ^2 values and better linear fits of the parameter r_c and β , as function of (E, θ). In Tab.3 we report some typical values of the 2 parameters and we compare them with the corresponding XMM values.⁸ The PSF correction is applied by the task *xrtmkarf*, distributed within the HEADAS software (<http://swift.gsfc.nasa.gov/docs/swift/analysis>).

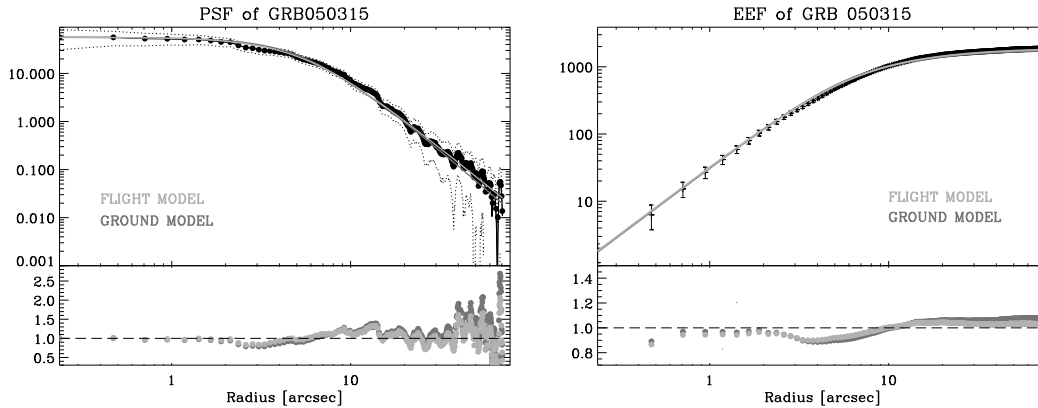


Figure 5. We compare the data from the second part of the observation of GRB050315 (without any pile-up) with the analytical model in order to perform an independent test. In the left panel we plot the PSF radial profile (log-log), normalized to the peak of the PSF. In the right panel we plot the EEF data and we compare it with the analytical function for the EEF (Eq. 2). In the lower panels we plot the ratio between the data and the model. We show also the comparison between the model built from the ground calibration and the updated model built by means of the in-flight calibration.

4.2. Testing the model

In order to test our model, we used the observation of GRB 050315. This is a very bright burst promptly observed by XRT in PC mode in manual state. The count rate registered by XRT, at the beginning of the observation (70 seconds from the trigger), was ~ 200 counts per second and ~ 0.7 counts per second after 400 seconds. Therefore in the first part of the observation (the first 400 seconds) the PSF was highly distorted by the pile-up effect and has to be corrected assuming the analytical model (see next Section); but from 400 seconds to the end of the observation the effect of the pile-up is negligible and the GRB is a very rich point-like source suitable for an independent check of the PSF analytical model. Using the model $\text{PSF}=\text{PSF}(E,\theta)$ for a grid of energy values we built a series of monochromatic images and summed them with the proper weights calculated from the normalized spectrum (for the energy grid we used a step of 100 eV ranging from 0.2 keV to 10.0 keV). The results of this procedure are shown in Fig.5. In the left panel we plot the PSF radial profile, normalized to the value of the peak of the PSF. In the right panel we plot the EEF data and we compare it with the analytical function for the EEF (Eq. 2). We find good agreement between the model and the data, which demonstrates that our goal is reached with a typical accuracy of 5%. In this figure we also show how the ground model compares with the flight data: the new in-flight model produces a slight improvement in the fit of the external parts of the PSF, beyond 20 arcseconds from the PSF centroid.

As an additional test for the PSF model we compared it with the Windowed Timing (WT) one-dimensional SB profile. The XRT supports different readout modes to enable it to cover the large dynamic range and rapid variability of the GRB afterglows. WT mode sacrifices part of the FOV and position information along one dimension in order to achieve high time resolution (1.7 ms) and mildly bright source spectroscopy (in the range 1-500 counts per second). For this test we considered the observation of the afterglow of the GRB 050502b: in this case the prompt observation registered a count rate between 10 and 100 counts per second during the first part of the observation. The WT image can be seen as a 2-dimensional image all accumulated on only one detector row. Therefore, as we did for the PC data in the previous case, we built a series of monochromatic images, summed them with the proper weights and then we accumulated the summed image on 1 row. The result of this procedure is shown in Fig.6: we find very good agreement between the model and the data in this case, as well.

4.3. Using the model

One of the most important applications of the predictive model of the PSF is the calculation of the PSF correction in presence of pile-up. In the usual case when the pile-up is negligible, the PSF correction is used to calculate

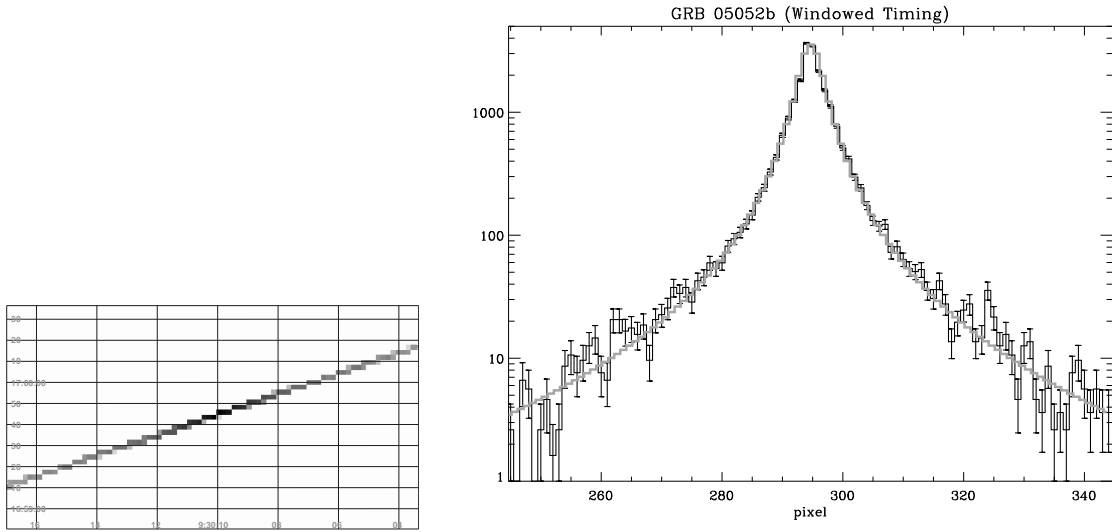


Figure 6. The analytical model can also be used for the WT data, where only one spatial dimension is registered by the XRT detector. On the left panel the sky image of the WT observation of GRB05052b is shown. The data are all registered in one detector row and it is rotated in order to have the north up and the east to the left. On the right panel the data (black) are compared to the model (grey). The pixel size is 2.36 arcseconds.

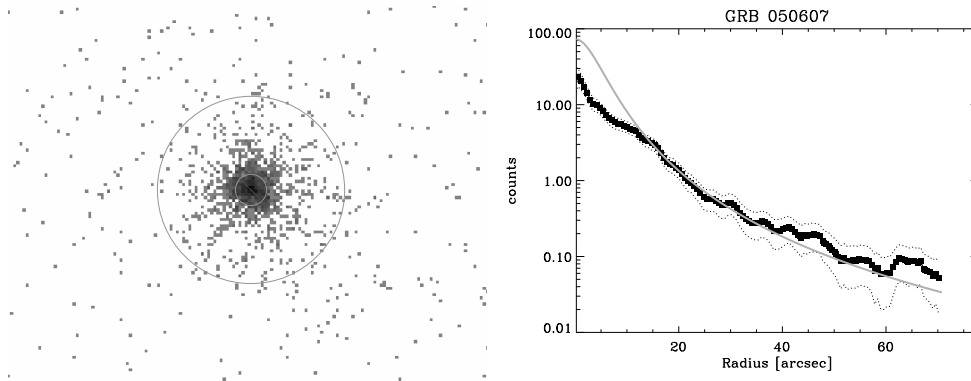


Figure 7. The afterglow of the GRB 050607. To analyze this source we could not use the standard extraction region (a 20 pixel circle), but we used an annulus with an inner radius of 6 pixels (left panel). In fact the PSF profile (black circles in the right panel) is distorted in the central 6 pixels by pile-up. To compare the data and the model (grey line in the right panel) we normalized the model to the value of the radial profile at the 7th pixel. The dotted lines are the error at 90% confidence

what fraction of the flux falls outside the region of the field of view considered for the analysis of a point like source: typically for the standard 20 pixels circle the excluded fraction is 10%. But in some particular cases, when pile-up is not negligible, to get rid of the affected data, we have to use a more complex geometry for the extraction region, typically an annulus with an inner radius of 3-7 pixels. In this case the PSF correction can be at the 300% and an accurate knowledge of the core of the PSF is mandatory. In the case of GRB 050607 the PC prompt observation is highly affected by pile-up and the PSF is distorted in its central part, up to 6 pixels ($\sim 15''$, Fig. 7). In this case the analysis of the light curve and the spectrum can only be performed within an annulus with an inner radius of 6 pixels, as shown in Fig.7. We proceeded as we did in the cases described in the previous section and from the reconstructed PSF image we calculated the PSF correction as the inverse of the fraction of the flux fallen outside the annulus, which corresponds to $\sim 71\%$.

5. CONCLUSIONS

We reported the results of the PSF calibration of the XRT telescope immediately after the verification and calibration phase. The in-flight calibrations are well consistent with the expectations from the on-ground end-to-end tests. In particular, we showed that the the XRT field of view is highly homogeneous in terms of imaging performances up to 8 arcminutes from the optical axis, thus accomplishing its primary scientific task, which is the prompt observation of the early X-ray GRB afterglows. Moreover, through the detailed study of the PSF and the analytical model we demonstrated that we can calculate the PSF correction of the instrument with good accuracy for astronomical sources. All the results of this study are implemented in the standard public software.

REFERENCES

1. N. Gehrels, G. Chincarini, P. Giommi, K. O. Mason, J. A. Nousek, A. A. Wells, N. E. White, S. D. Barthelmy, D. N. Burrows, L. R. Cominsky, K. C. Hurley, F. E. Marshall, P. Mészáros, P. W. A. Roming, L. Angelini, L. M. Barbier, T. Belloni, S. Campana, P. A. Caraveo, M. M. Chester, O. Citterio, T. L. Cline, M. S. Cropper, J. R. Cummings, A. J. Dean, E. D. Feigelson, E. E. Fenimore, D. A. Frail, A. S. Fruchter, G. P. Garmire, K. Gendreau, G. Ghisellini, J. Greiner, J. E. Hill, S. D. Hunsberger, H. A. Krimm, S. R. Kulkarni, P. Kumar, F. Lebrun, N. M. Lloyd-Ronning, C. B. Markwardt, B. J. Mattson, R. F. Mushotzky, J. P. Norris, J. Osborne, B. Paczynski, D. M. Palmer, H.-S. Park, A. M. Parsons, J. Paul, M. J. Rees, C. S. Reynolds, J. E. Rhoads, T. P. Sasseen, B. E. Schaefer, A. T. Short, A. P. Smale, I. A. Smith, L. Stella, G. Tagliaferri, T. Takahashi, M. Tashiro, L. K. Townsley, J. Tueller, M. J. L. Turner, M. Vietri, W. Voges, M. J. Ward, R. Willingale, F. M. Zerbi, and W. W. Zhang, "The Swift Gamma-Ray Burst Mission," *The Astrophysical Journal* **611**, pp. 1005–1020, 2004.
2. S. D. Barthelmy and et al., "Burst Alert Telescope (BAT) on the Swift MIDEX mission," *Space Science Review* **120**, p. in press, 2005.
3. D. N. Burrows and et al., "The Swift X-Ray Telescope," *Space Science Review* **120**, p. in press, 2005.
4. P. W. Roming and et al., "The Swift Ultra-Violet/Optical telescope," *Space Science Review* **120**, p. in press, 2005.
5. A. Moretti, S. Campana, G. Tagliaferri, A. F. Abbey, R. M. Ambrosi, L. Angelini, A. P. Beardmore, H. W. Bräuninger, W. Burkert, D. N. Burrows, M. Capalbi, G. Chincarini, O. Citterio, G. Cusumano, M. J. Freyberg, P. Giommi, G. D. Hartner, J. E. Hill, K. Mori, D. C. Morris, K. Mukerjee, J. A. Nousek, J. P. Osborne, A. D. T. Short, F. Tamburelli, D. J. Watson, and A. A. Wells, "Swift XRT point spread function measured at the Panter end-to-end tests," *Proc. SPIE* **5165**, pp. 232–240, 2004.
6. J. E. Hill, D. N. Burrows, J. A. Nousek, A. F. Abbey, R. M. Ambrosi, H. W. Bräuninger, W. Burkert, S. Campana, C. Cheruvu, G. Cusumano, M. J. Freyberg, G. D. Hartner, R. Klar, C. Mangels, A. Moretti, K. Mori, D. C. Morris, A. D. T. Short, G. Tagliaferri, D. J. Watson, P. Wood, and A. A. Wells, "Readout modes and automated operation of the Swift X-ray Telescope," *Proc. SPIE* **5165**, pp. 217–231, 2004.
7. P. Romano and et al., "Swift XRT Effective area," *Proc. SPIE*, 2005.
8. A. Read, "PSF of the X-ray telescope," *XMM-CCF-REL-167*, 2004.